Supplementary Information

Ultralow-Loaded Molybdate on Defect-Engineered g-C_3N_4 for Efficient Electrochemical Nitrate Reduction to Ammonia

Debasish Halder,[a] Nandita Mohandas,[b] Rupam Ghosh,[c] Takefumi Yoshida,[d] Tharangattu N. Narayanan,[b] Pralay K. Santra,[c] Sounak Roy*[a]

a. Department of Chemistry, Birla Institute of Technology and Science (BITS) Pilani, Hyderabad Campus, India

b. Tata Institute of Fundamental Research-Hyderabad, Hyderabad, India

c. Centre for Nano and Soft Matter Sciences (CeNS), Bengaluru, India

d. Graduate School of Systems Engineering, Wakayama University, Japan

1. Reagents

For the synthesis of g-C_3N_4, melamine (Sigma-Aldrich) and urea (SRL Pvt. Ltd.) were used as precursors. Sodium molybdate dihydrate ($Na_2MoO_4 \cdot 2H_2O$; SD Fine Chem Ltd., India) served as the metal precursor for catalyst synthesis. Isopropanol (IPA) and ethanol (EtOH), both obtained from SRL Pvt. Ltd., were used as solvents. A 5 wt% Nafion solution (Sainergy Fuel Cell India Pvt. Ltd.) was employed as a binder for the working electrode. Potassium hydroxide (KOH; SRL Pvt. Ltd.) was used as the anolyte, while potassium nitrate (KNO_3; Sigma-Aldrich) was used as the nitrate source. For ammonia and nitrite calibration, ammonium chloride (NH_4Cl; SD Fine Chem Ltd., India) and potassium nitrite (KNO_2; Sigma-Aldrich) were used, respectively. Product analysis was carried out using sodium hydroxide (NaOH; SRL Pvt. Ltd.), salicylic acid ($C_7H_6O_3$; Sigma-Aldrich), sodium citrate tribasic dihydrate ($Na_3C_6H_5O_7 \cdot 2H_2O$; SRL Pvt. Ltd.), sodium hypochlorite pentahydrate ($NaClO \cdot 5H_2O$; TCI), sodium nitroferricyanide ($C_5FeN_6Na_2O$; SRL Pvt. Ltd.), N-(1-naphthyl)ethylenediamine dihydrochloride ($C_{12}H_{14}N_2 \cdot 2HCl$; Sigma-Aldrich), sulfanilamide ($H_2NC_6H_4SO_2NH_2$; Sigma-Aldrich), and phosphoric acid (H_3PO_4; SRL Pvt. Ltd.). All chemicals were used as received without further purification. All solutions were prepared using ultrapure water (Milli-Q).

2. Synthesis of Catalysts

2.1 Synthesis of bulk-g-C_3N_4

Bulk-g-C_3N_4 (B-gCN) was synthesised via a precursor-reforming strategy from a previously reported method.[1] Specifically, urea (8 g) and melamine (6 g) were each dissolved in 70 mL of deionized water, taken in a 100 mL Teflon-lined stainless-steel autoclave and the mixture was stirred for 1 hour to obtain a homogeneous suspension. The resulting mixture was then subjected to hydrothermal treatment at 180 °C for 24 hours. After cooling to room temperature, the intermediate product was collected, thoroughly washed with deionised water, and dried in an oven at 100 °C for 12 hours. Finally, the dried solid was ground into fine powder and calcined at 550 °C at a rate of 2.3 °C min^{-1} for 2 hours to yield a yellow bulk-g-C_3N_4 powder.

2.2 Synthesis of Exfoliated-Nitrogen vacant-g- C_3N_4

Exfoliated nitrogen-vacancy-rich g-C_3N_4 (ENv-gCN) was synthesized via a two-step process. In the first step, bulk g- C_3N_4 (B-gCN) was acid-etched to obtain chemically exfoliated g-C_3N_4. In the second step, nitrogen vacancies were introduced to yield ENv-gCN. Specifically, 500 mg of B-gCN was dispersed in 8 mL of concentrated H_2SO_4 and heated at 100 °C under continuous stirring for 16 h. The resulting clear solution was then diluted with 2 L of deionized

water to form a white slurry. The slurry was filtered and washed repeatedly with deionized water until a neutral pH (≈7) was reached, followed by drying at 100 °C for 12 h to obtain E-gCN. Subsequently, 200 mg of the as-prepared E-gCN was thermally etched in a tubular furnace at 600 °C for 2 h under an argon atmosphere to generate nitrogen vacancies, yielding ENv-gCN.

2.3 Synthesis of Mo/B-gCN and Mo/EN-gCN

150 mg of B-gCN and 50 mg of sodium molybdate were dispersed in 60 mL of isopropyl alcohol and stirred for 30 minutes. The mixture was then subjected to solvothermal treatment in a 100mL Teflon-lined autoclave for 24 hours at 180 °C. The cooled mixture was then filtered and dried at 80 °C for 12 hours and denoted as Mo/B-gCN. In a similar manner, Mo/ENv-gCN was prepared by mixing 150 mg of ENv-gCN with 5 mg of sodium molybdate in 60 mL of isopropyl alcohol.

3. Material characterization

The structure and crystalline nature of the synthesized catalysts were assessed through X-ray diffraction (XRD) analysis performed on a Rigaku Ultima IV apparatus employing Cu Kα radiation. The X-ray absorption fine structure (XAFS) measurements for the powder sample pellet were conducted at the NW10A beamline of the PF-AR, operated by the High Energy Accelerator Research Organization (KEK), under proposal no. 2023G598. The X-ray was monochromatized by an Si (311) water-cooled double crystal monochromator. Rh coated Double flat mirror was employed for higher harmonics reduction. Mo foil was employed to calibrate the Mo K-edge. Subsequently, the XAFS data underwent processing using the ATHENA program. The surface morphology and composition analyses were conducted using a field emission scanning electron microscopy system (FE-SEM, FEI-Apreo S) equipped with an energy dispersive spectroscopy (EDS) unit. The instrument was operated at an acceleration voltage of 20 kV. X-Ray photoelectron spectroscopy (XPS) of the synthesized materials was performed using a Thermo Scientific K-Alpha surface analysis spectrometer with Al Kα radiation (1486.6 eV). The data profiles were subjected to a nonlinear least-squares curve fitting program with a Gaussian–Lorentzian production function and processed with Avantage software. The binding energies (BE) of all the XPS data were calibrated *vs.* the standard C 1s peak at 284.8 eV. The EPR spectra were measured at room temperature using Bruker ESR 5000. The UV/Vis spectra for ammonia and nitrite quantification were measured using Jasco

V-670 spectrophotometer. The FTIR spectra of the synthesized samples were collected using a Bruker Alpha II spectrometer.

4. Electrocatalysis Measurements

Electrochemical measurements were performed using an OrigaFlex-OGF500 potentiostat at room temperature. Nitrate reduction was evaluated in a H-type electrochemical cell employing a three-electrode configuration, comprising an activated carbon cloth electrode drop-cast with the catalyst as the working electrode, an Ag/AgCl (sat. KCl) reference electrode, and a Pt wire counter electrode. All potentials measured versus Ag/AgCl (sat. KCl) were converted to the reversible hydrogen electrode (RHE) scale using the relation: $E_{(RHE)} = E_{(Ag/AgCl)} + 0.0591 \times pH + 0.197$ V. For catalyst ink preparation, 2 mg of the synthesized catalyst was dispersed in a mixture of 1 mL isopropanol (IPA) and 20 µL Nafion binder, followed by ultrasonication for 1 h. Subsequently, 100 µL of the ink was drop-casted onto the activated carbon cloth electrode. Electrochemical testing was conducted in an electrolyte containing 50 mL of 0.5 M KNO_3 and 0.5 M KOH mixture (pH ≈ 14) as catholyte and 50 mL 0.5 M KOH as anolyte. Prior to measurements, the electrolyte was purged with Ar for 15 min to remove dissolved O_2 and N_2. Linear sweep voltammetry (LSV) was recorded from 0.17 to −1.02 V vs. RHE at a scan rate of 10 mV s^{-1} to assess the catalytic activity toward nitrate reduction. Chronoamperometric measurements were subsequently performed for 2 h to evaluate the electrocatalytic stability and nitrate reduction performance. Electrochemical impedance spectroscopy (EIS) was carried out using a BioLogic SP-150 CV instrument with an AC perturbation applied over the frequency range of 0.01 Hz to 100 kHz. The electrochemically active surface area (ECSA) was determined from the electrochemical double-layer capacitance (C_{dl}) according to the formula, ECSA = C_{dl} / C_s. C_{dl} values were obtained from cyclic voltammograms collected in the non-faradaic region (0.97 to1.37 V vs. RHE) in 1 M KOH at scan rates ranging from 20 to 120 mV s^{-1} (Fig. S8a, 8c). The capacitive current, arising from double-layer charging and proportional to the electroactive surface area, was extracted from the slope of the plot of half the capacitive current, $\Delta J/2 = (J_{anodic} - J_{cathodic})/2$, versus the scan rate. Representative C_{dl} values for the prepared catalysts are shown in Fig. S8b and 8d). The specific capacitance (C_s) was calculated using the following equation, $Cs = \frac{\int Vdv}{m \times Vs \times \Delta V}$., where, $\int Vdv$ is (mA mV^{-1}) corresponds to the integrated area under the CV curve at 10 mV s^{-1}, m (=0.2 mg) is the catalyst loading on the electrode (geometric area =

1 cm^2), v is the scan rate (mV s^{-1}), and ΔV is the potential window (mV). The resulting C_s values, normalized to catalyst mass (mF mg^{-1}), were further converted to mF cm^{-2}. To explore the kinetics of the NO_3RR, Tafel plots were also plotted.

5. Determination of products and intermediates

5.1 Ammonia detection and quantification

The concentration of ammonia was determined using the indophenol blue (IB) spectrophotometric method. Three stock solutions were prepared: solution A, containing 5 g of sodium salicylate and 2 g of NaOH dissolved in 100 mL of deionized water; solution B, prepared by dissolving 1.25 g of trisodium citrate in 25 mL of deionized water followed by the addition of 200 mg of sodium hypochlorite (NaOCl); and solution C, prepared by dissolving 150 mg of sodium nitroferricyanide dihydrate in 25 mL of deionized water. For analysis, 100 µL of the post-reaction electrolyte was diluted with 2 mL of 1 M NaOH, after which 1 mL of solution A, 1 mL of solution B, and 400 µL of solution C were added sequentially. The mixture was allowed to stand under ambient conditions for 2 h prior to recording the UV/vis absorption spectrum in the 550-850 nm range using a spectrophotometer. A calibration curve was obtained using standard ammonium chloride (NH_4Cl) solutions.

5.2. Nitrite detection and quantification

Nitrite concentration in the post-reaction electrolyte was determined using the Griess colorimetric method. The Griess reagent was prepared by dissolving 0.2 g of *N*-(1-naphthyl)-ethylenediamine dihydrochloride, 4.0 g of sulfanilamide, and 10 mL of H_3PO_4 in 50 mL of deionized water. For measurement, the 50 µL of the post-reaction electrolyte was diluted to 4 mL of DI water, followed by the addition of 20 µL of the Griess reagent. After waiting for 20 minutes at room temperature to allow colour development, the UV/vis absorption spectrum was recorded in the 440-650 nm range. A calibration curve was constructed by plotting the absorbance at 540 nm as a function of nitrite concentration using standard potassium nitrite (KNO_2) solutions, from which the nitrite concentration in the analyte was determined.

6. Faradaic efficiency (FE) and yield rate calculation

FEs for NH_3 and NO_2^- in terms of % have been calculated using the following equations

$$FE_{Ammonia} = \frac{q}{Q} \times 100\ \% = \frac{n \times c \times V \times F}{17 \times Q} \times 100\ \% \qquad (1)$$

$$FE_{Nitrite} = \frac{q}{Q} \times 100\ \% = \frac{n \times c \times V \times F}{46 \times Q} \times 100\ \% \quad (2)$$

Here, Q is the total charge passed during electrolysis, n represents the number of electrons transferred (n=8 for ammonia formation and n=2 for nitrite formation from nitrate), c is the concentration of product generated, V is the catholyte volume in the cathode chamber, and F is the Faraday constant (96485 C mol^{-1}).

Yield rates of ammonia and nitrite have been calculated per unit time and per unit catalyst mass loading expressed as mmol h^{-1} mg^{-1} using the following formula.

$$Yield\ rate = \frac{c \times V}{m \times t} \quad (3)$$

Here, 'm' represents the loading mass of catalysts, and 't' is the electrolysis time.

7. In-situ SHINERS studies

In-situ shell-isolated nanoparticle-enhanced Raman spectroscopy (SHINERS) was carried out to investigate the electrochemical NO_3^- reduction to NH_3 under the applied potentials in a customized air-tight in-situ Raman electrochemical cell, where the catalyst coated carbon cloth was used as the working electrode. A neat layer of silica-coated gold nanoparticles (SiO_2@Au) were drop-casted onto the electrode to enhance Raman scattering while preventing catalytic and electronic interaction between the plasmonic gold core and the electrolyte. It was subjected to plasma treatment followed by thermal annealing to remove residual organic contaminants and ensure a clean, impurity-free and reproducible surface.[2] Control cyclic voltammetry (CV) experiments were performed in the presence and absence of SiO_2 coating over Au nanoparticles (AuNP) and the electrochemical behaviour as shown in Fig.S9 confirmed that the SiO_2 shell over the AuNP completely masked their electronic and electrochemical properties. AuNP clearly shows oxidation and reduction peaks in the CV pattern, but when coated with SiO_2 shell the peaks disappear. Therefore, AuNP served exclusively as Raman signal enhancers and did not participate in the catalytic process. The SHINERS data were obtained using a Renishaw inVia Raman Microscope with 532 nm laser excitation using L50x lens. The time for recording data is optimized to 10 s for a better signal-to-noise ratio.

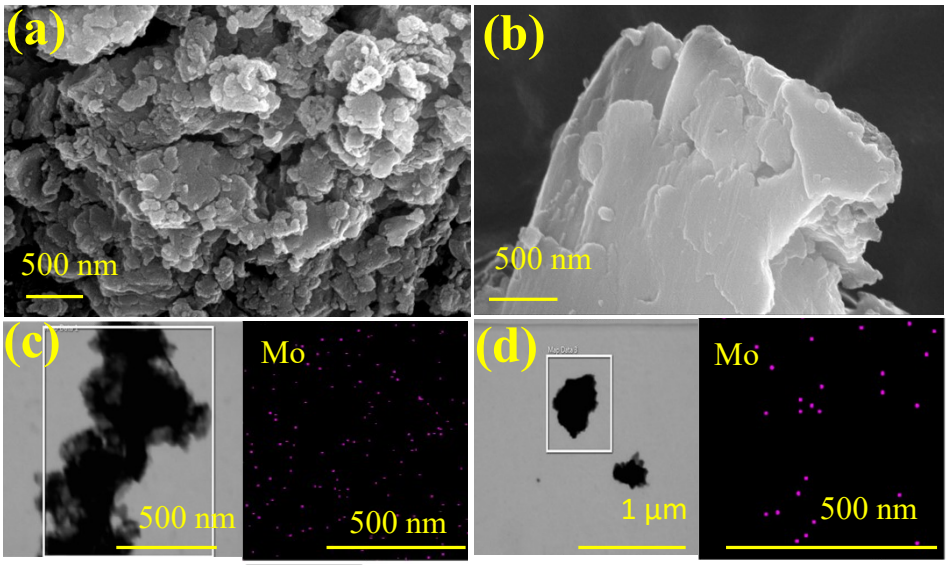

Fig. S1. SEM images of (a) B-gCN, (b) ENv-gCN, elemental mapping images of (c) Mo/B-gCN, (d) Mo/ENv-gCN.

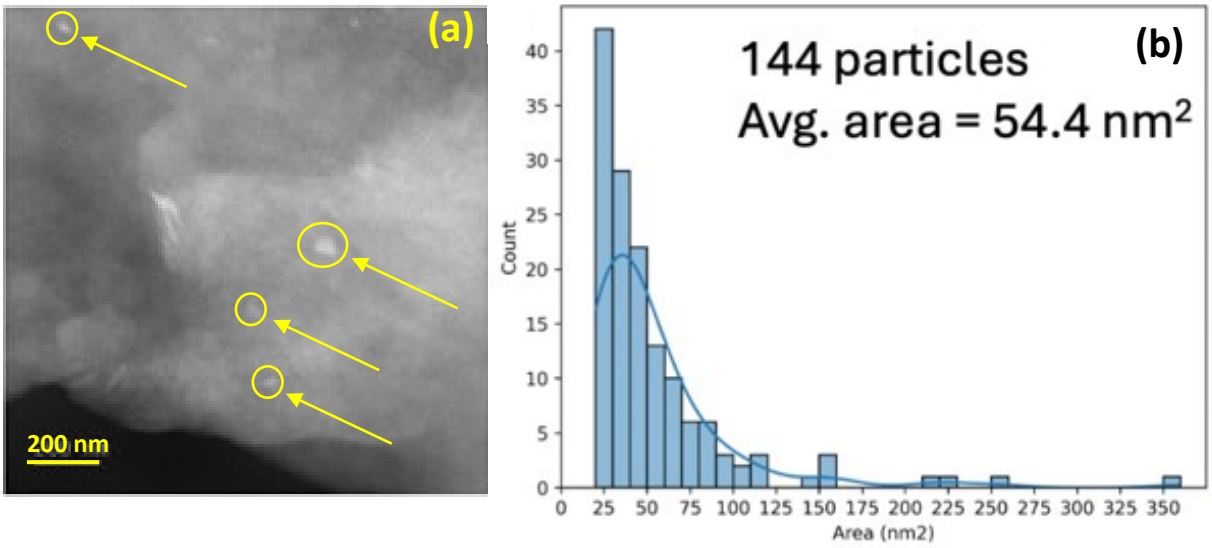

Fig. S2. (a) Bright-field TEM image of Mo/B-gCN showing Mo clusters, (b) particle size analysis of Mo nanoclusters in Mo/ENv-gCN.

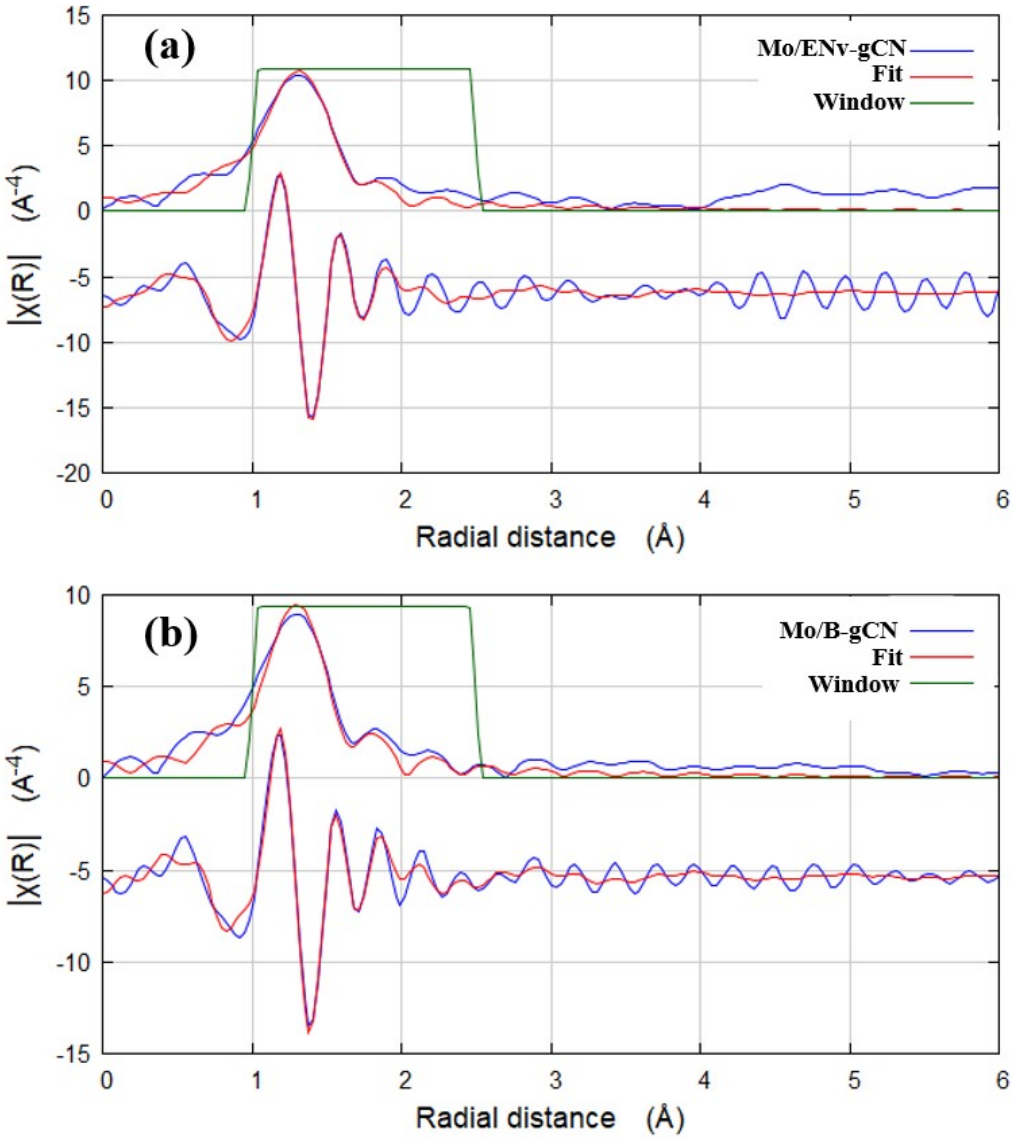

Fig. S3. Fitting results of the EXAFS spectra of (a) Mo/ENv-gCN, and (b) Mo/B-gCN.

Table S1: Structural parameters extracted from Mo K-edge EXAFS fitting within a k-range of 30 – 120 nm^{-1} and a fixed $S_0^2 = 1.098$ (as obtained from Mo foil).

Sample	Scattering pair	CN	R (nm)	σ^2 (10^{-5} nm^2)	ΔE_0 (eV)
Mo/B-gCN	Mo-O	4.1±1.6	0.178±0.021	5.2±2.7	-3.3± 5.6
	Mo-O	1.3±1.5	0.207±0.033		
Mo/ENv-gCN	Mo-O	5.8±3.3	0.179±0.030	7.1±4.1	-4.5± 6.8
	Mo-O	2.3±2.9	0.211±0.038		

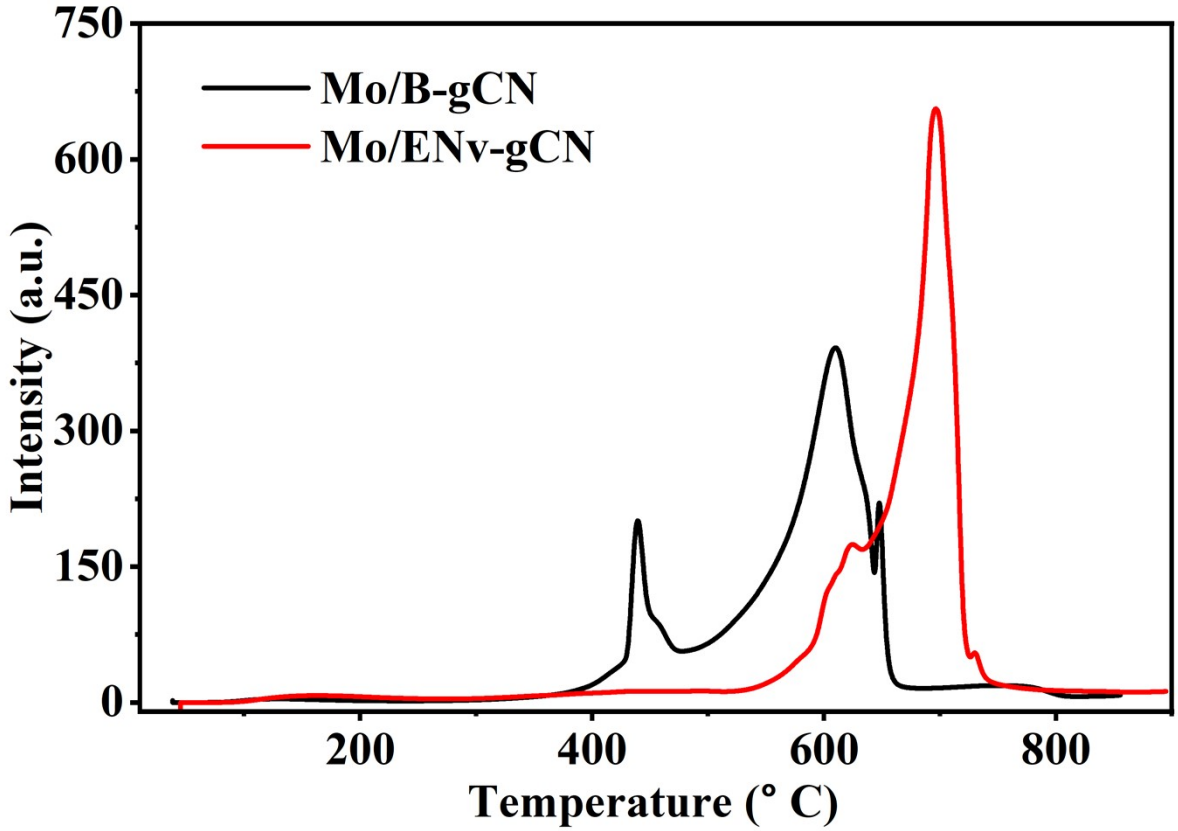

Fig. S4. NH_3-Temperature Programmed Desorption (NH_3-TPD) plot for both catalysts.

NH_3-TPD analysis:

NH_3-TPD was performed on both catalysts to elucidate the role of Mo mixed valence states Mo^{6+}/$Mo^{5+}$and associated Lewis acidity in the catalytic mechanism. As shown in the TPD profiles, Mo/ENv-gCN exhibits markedly higher desorption intensities relative to Mo/B-gCN, translating to a substantially greater total ammonia uptake of 17351 μmol/g_{cat} compared to 13915 μmol/g_{cat} for Mo/B-gCN. Beyond the quantitative difference in acid site density, the NH_3 desorption peak of Mo/ENv-gCN is shifted approximately 100 °C toward higher temperatures, indicative of a greater population of stronger Lewis acid sites relative to Mo/B-gCN. The enhanced Lewis acid strength and higher ammonia uptake capacity of Mo/ENv-gCN are attributed to its lower Mo^{6+}/ Mo^{5+} ratio compared to Mo/B-gCN.[3] In molybdate systems, Mo^{5+} centers (d^1 configuration) exhibit moderate-to-strong Lewis acidity and a higher propensity for Lewis base coordination than fully oxidized Mo^{6+} (d^0), owing to their favourable charge density and partially occupied frontier orbitals that facilitate adsorbate interaction through combined electrostatic and orbital contributions.[4–5] Consequently, the greater availability of Mo^{5+} sites in Mo/ENv-gCN provides a higher density of optimal Lewis acid centres for nitrate adsorption, activation, and stepwise reduction. These findings collectively suggest that Mo^{5+} site availability is a key determinant of both the selectivity and efficiency of the electrochemical nitrate-to-ammonia reduction pathway.

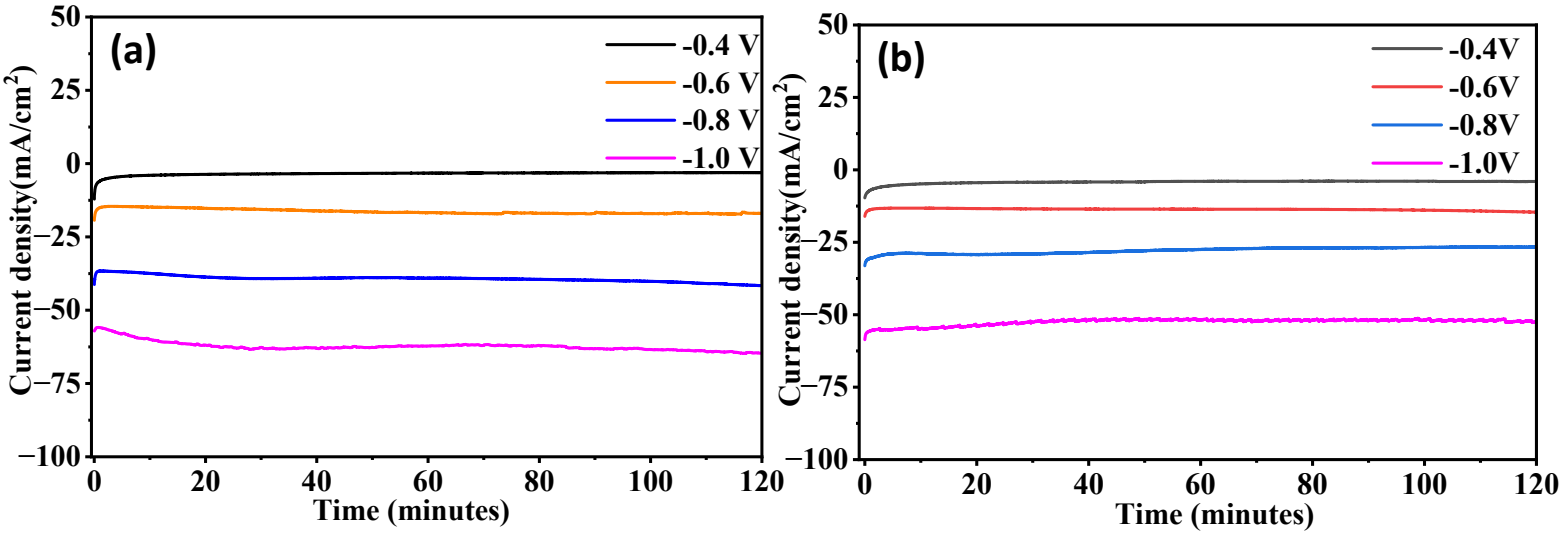

Fig. S5. Chronoamperometric studies in 0.5(M) KOH + 0.5 (M) KNO_3 for (a) Mo/ENv-gCN and (b) Mo/B-gCN

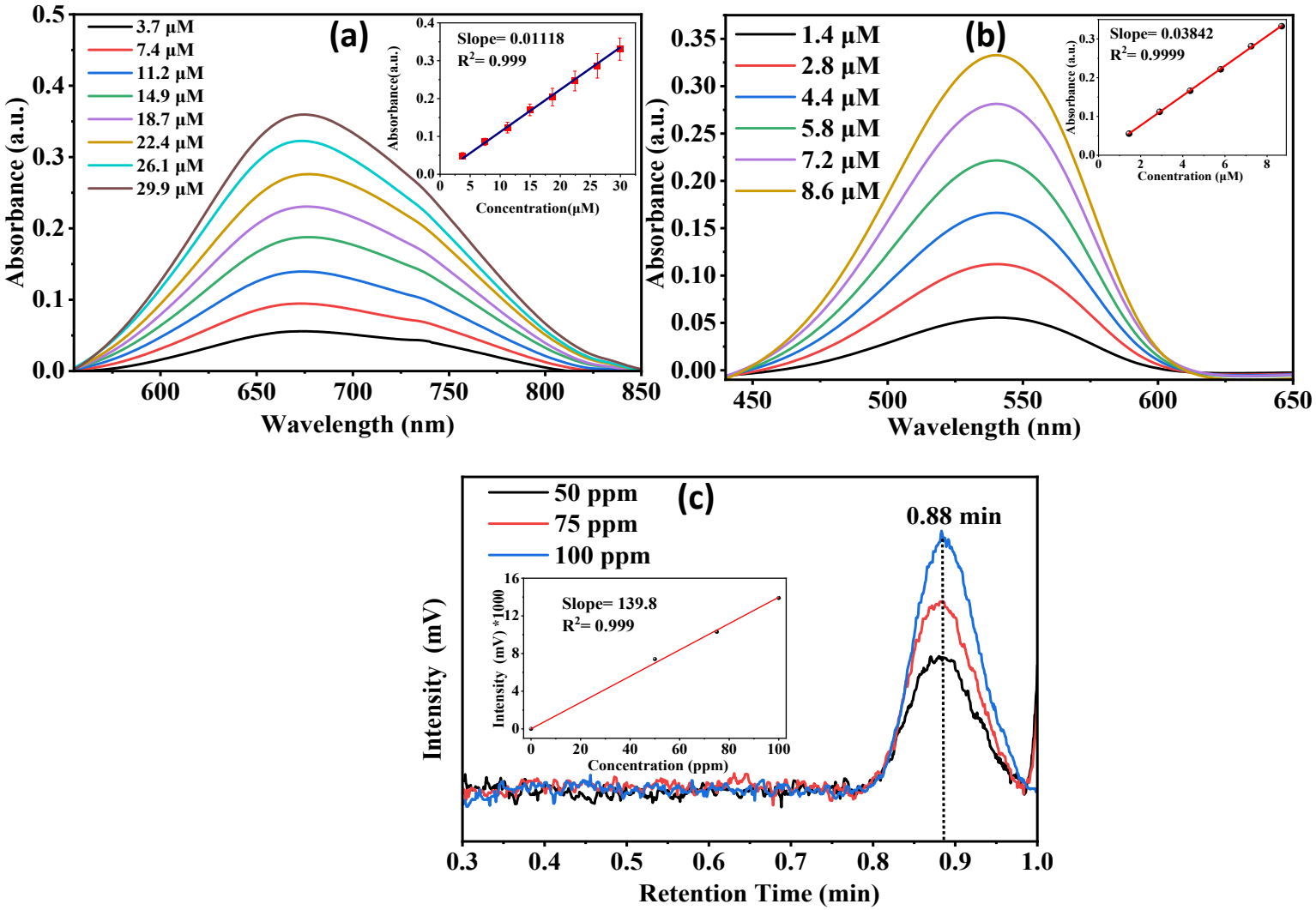

Fig. S6. (a) UV-Vis absorption spectra for NH_3 detection by the indophenol blue method, (b) UV-Vis absorption spectra for NO_2^- detection by the Griess test, (c) chromatogram for H_2 detection showing H_2. The inset shows the corresponding calibration plot.

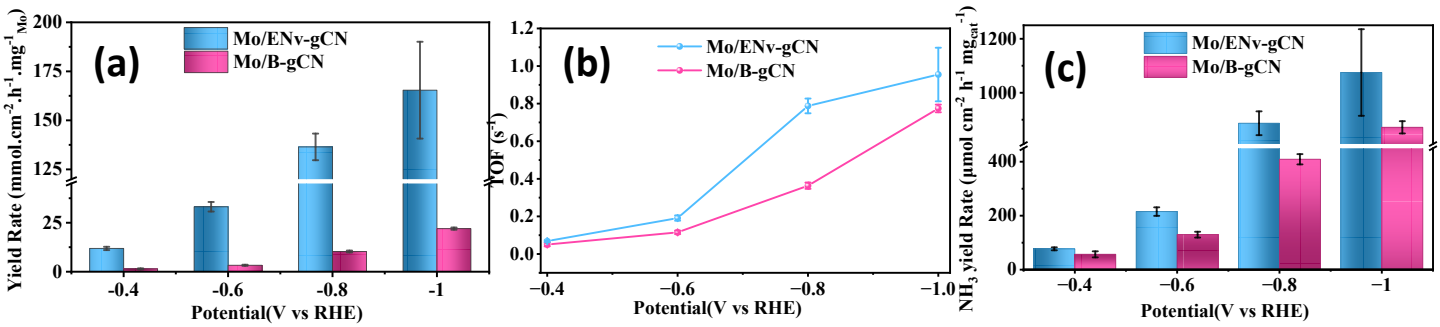

Fig. S7. (a) Ammonia yield rate normalised to geometric area of working electrode and unit Mo loading, (b) turnover frequency (TOF), (c) ammonia yield rate normalised to geometric area of working electrode and unit catalyst mass loading for both Mo/ENv-gCN and Mo/B-gCN catalysts.

The electrocatalytic nitrate-to-ammonia production performance of Mo/ENv-gCN and Mo/B-gCN was systematically evaluated using additional metrics, including geometric current density and turnover frequency (TOF), to enable the comparison. As shown in Fig. S7b, TOF of both catalysts increased progressively with increasingly negative applied bias, with Mo/ENv-gCN demonstrating superior catalytic activity, achieving a TOF of approximately 1.0 s^{-1} at −1.0 V vs. RHE, compared to ~ 0.77 s^{-1} for Mo/B-gCN under the same applied bias. Correspondingly, the NH_3 yield rate, normalised to geometric area of working electrode and unit catalyst mass loading (Fig. S7c) followed a similar trend, wherein Mo/ENv-gCN Mo/EN-gCN delivers significantly higher ammonia production rates than Mo/B-gCN at all investigated potentials, exhibiting a markedly enhanced ammonia production rate of ~1075 μmol cm^{-2} h^{-1} mg_{cat}^{-1} at −1.0 V vs. RHE, compared to Mo/B-gCN (~870 μmol cm^{-2} h^{-1} mg_{cat}^{-1}) under identical conditions. To contextualise the present work, a comparison table is provided here (Table S2).

Table S2: Comparison of the NO_3RR activity for Mo/ENv-gCN with other electrocatalysts in aqueous electrolytic solution at ambient conditions

Catalyst	Electrolyte	NH_3 yield	FE (%)	References
Cu-NB-100	0.1 M PBS/500 ppm NO_3^-	650 mmol h^{-1} g_{cat}^{-1}	95.3	[6]
Fe-Mo DSAC	1 M KOH/0.1 M KNO_3	13.56 mg cm^{-2} h^{-1}	94	[7]
Fe/Cu-HNG	1 (M) KOH and 0.1 (M) KNO_3	1.08 mmol h^{-1} mg^{-1}	92.5	[8]
a_1-Ru/CNTs	5 m(M) Cs_2CO_3/500 ppm NO_3^-	145.1 μg h^{-1} mg_{cat}^{-1}	80.62	[9]
Fe_2TiO_5	PBS/0.1 M $NaNO_3$	0.73 mmol h^{-1} mg_{cat}^{-1}	87.6	[10]
CoP NRs	0.5 M Na_2SO_4/50 mM $NaNO_3$	30.1 mg h^{-1} mg_{cat}^{-1}	97.1	[11]
1:2 MnPc : RGO	0.1 M K2SO4 + 0.2 M KNO3	20316 μg h^{-1} mg_{cat}^{-1}	98.3%	[12]
PCNV-600	0.5 M Na_2SO_4 + 100 ppm nitrate	0.03262 $mmol^{-1}$ g^{-1} h^{-1}	89.96	[13]
$Fe_2O_3/NiFe_2O_4$	0.1 M Na_2SO_4 + 0.1 M KNO_3	47.47 mg h^{-1} mg_{cat}^{-1}	94.10	[14]
PB-Co	0.5 M K_2SO_4 + 0.1 M KNO_3	995.5 ± 28.4 mmol h^{-1} mg_{cat}^{-1}	95.8 ± 1.06	[15]
CoNi–LDH@Cu_2O	0.1 M $NaNO_3$ + 1 M NaOH	75.2 mg h^{-1} cm^{-2}	97.8	[16]
Mo/ENv-gCN	0.5 M KNO_3 + 0.5 M KOH	1075 μg h^{-1} mg_{cat}^{-1}	80.6	This work

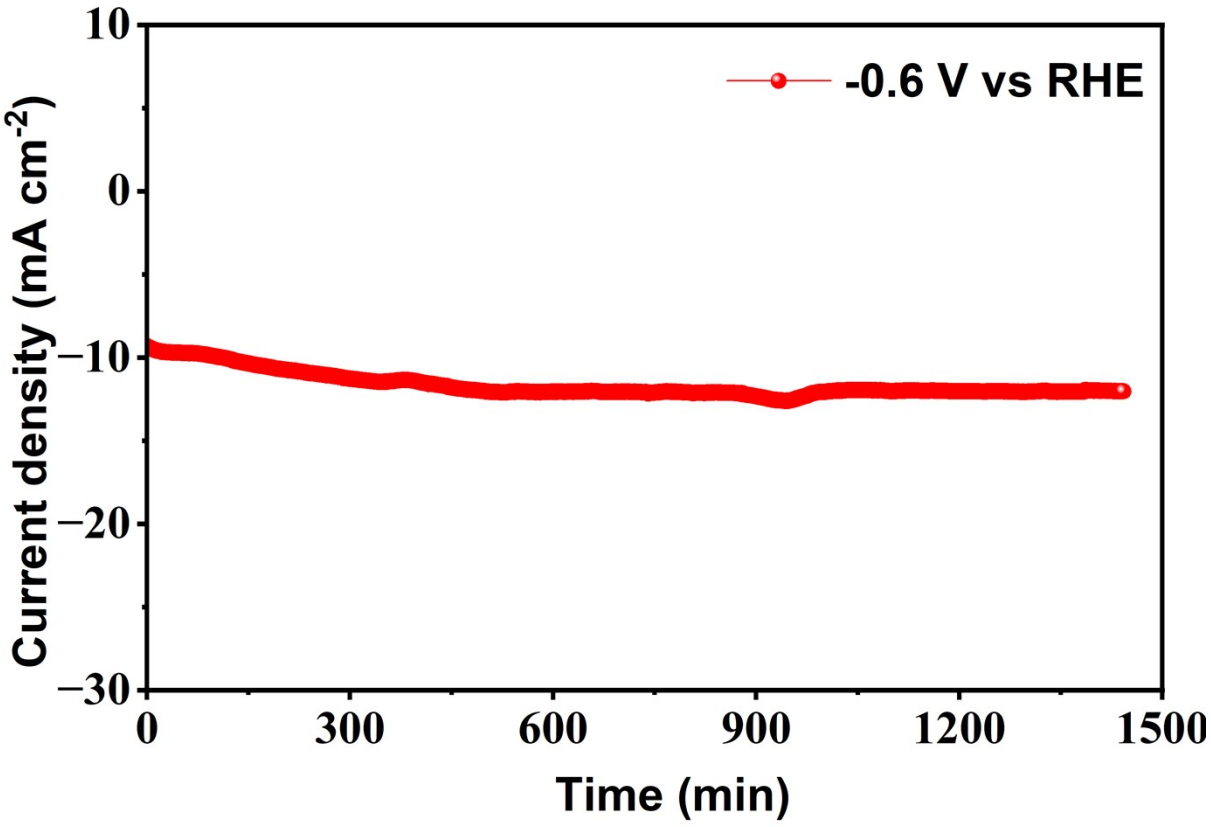

Fig. S8. 24h Chronoamperometric studies in 0.5(M) KOH + 0.5(M) KNO_3 for Mo/ENv-gCN

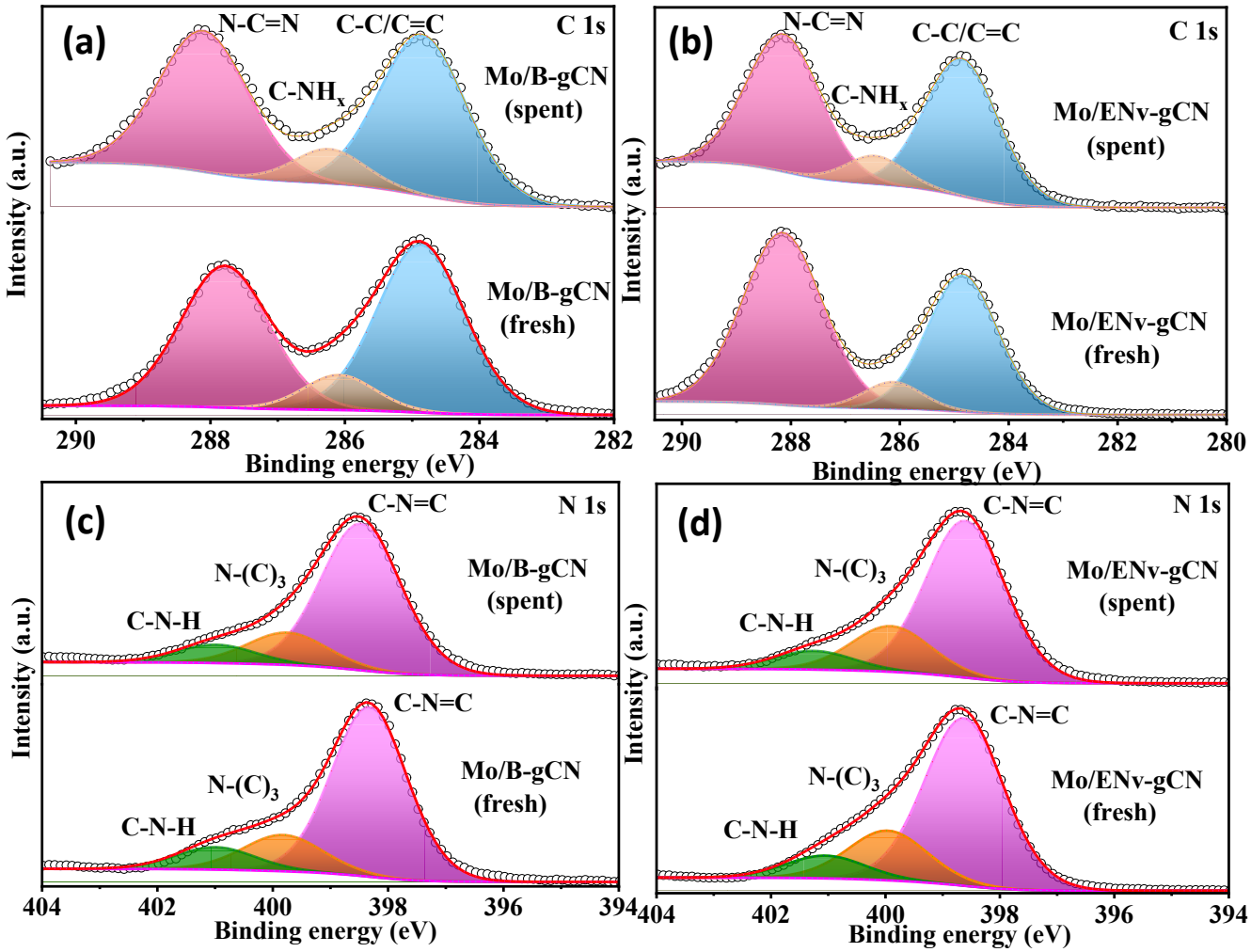

Fig. S9. C 1s core level XPS of (a) fresh and spent Mo/B-gCN, along with (b) fresh and spent Mo/ENv-gCN (b). N 1s core level XPS of (c) fresh and spent Mo/B-gCN, and (d) fresh and spent Mo/ENv-gCN.

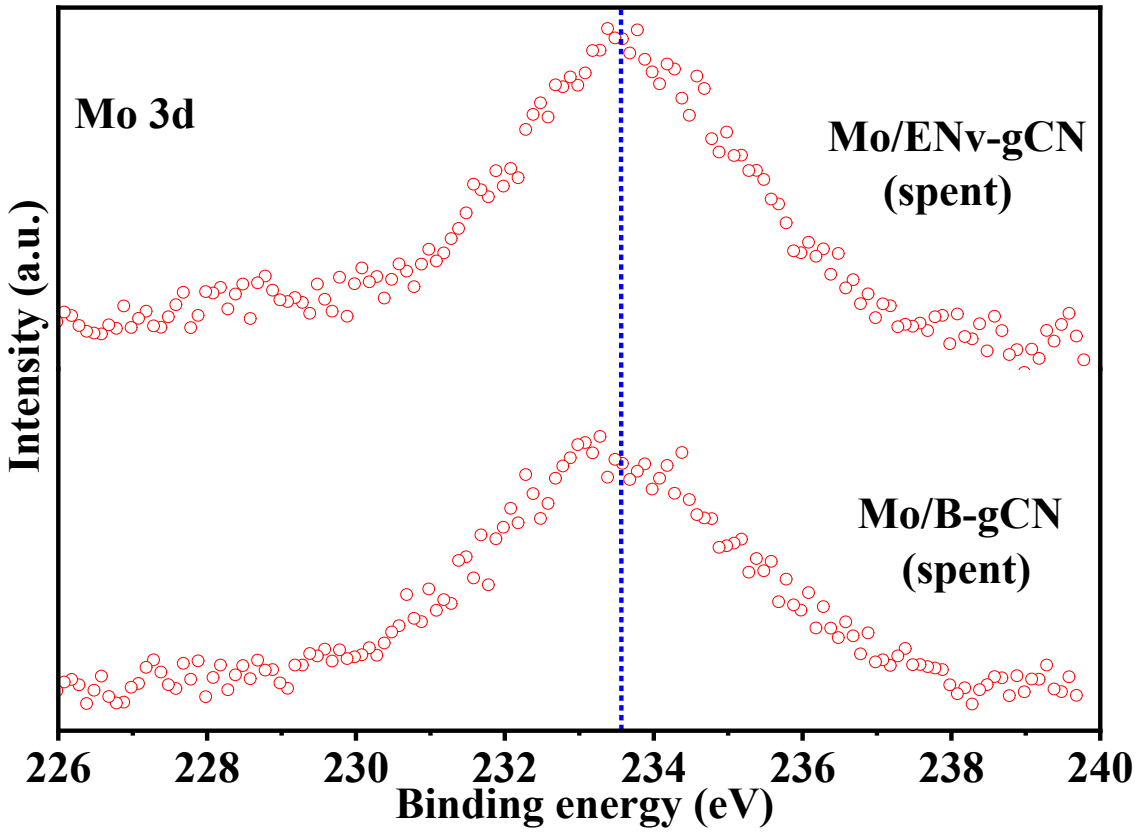

Fig. S10. Mo 3*d* core level XPS of both spent catalysts Mo/B-gCN and Mo/ENv-gCN.

XPS characterisation of spent catalysts:

A detailed XPS characterization of the spent Mo/B-gCN and Mo/ENv-gCN catalysts (in Fig. S8) reveal that the binding energies and peak positions of C 1*s* and N 1*s* for g-C_3N_4 functional groups i.e. N-C=N (~288 eV), C-N=C (~398 eV), and N-$(C)_3$ (~400 eV), remain largely unchanged after catalysis, with only minor shifts and intensity variations attributable to surface Mo interactions rather than bulk structural degradation. Post-catalysis Mo 3*d* XPS (Fig. S9) shows a broadened Mo 3*d* signal and a changed peak profile compared with the fresh sample (Fig. 2f), which we attribute to partial oxidation-state redistribution of Mo under reaction condition. However, the maintained activity over five cycles and the stable chronoamperometric response rather support the operational durability of the catalyst.

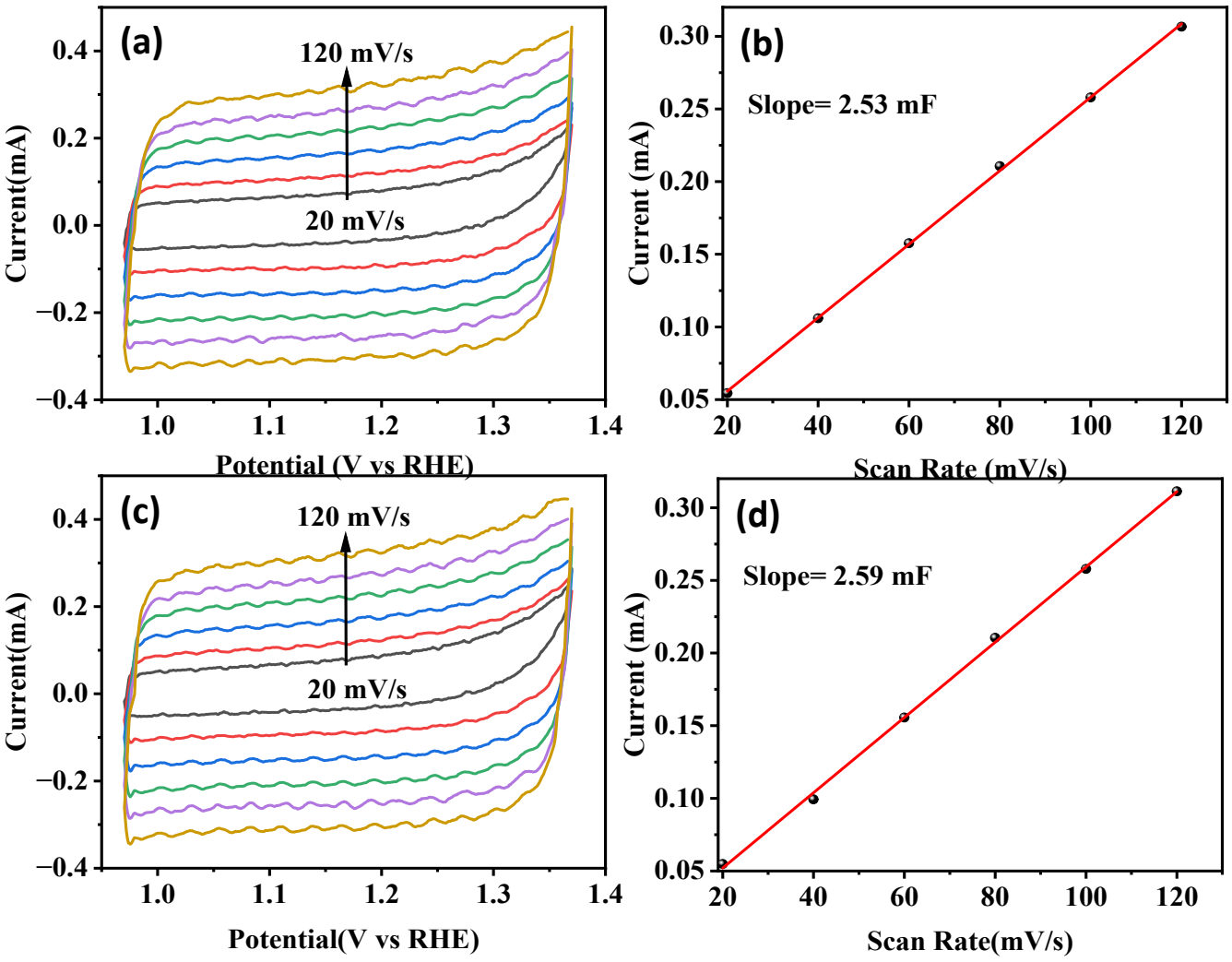

Fig. S11. (a) Scan rate plot and (b) double layer capacitance (C_{dl}) value for Mo/B-gCN, (c) scan rate plot and (d) double layer capacitance (C_{dl}) value for Mo/ENv-gCN

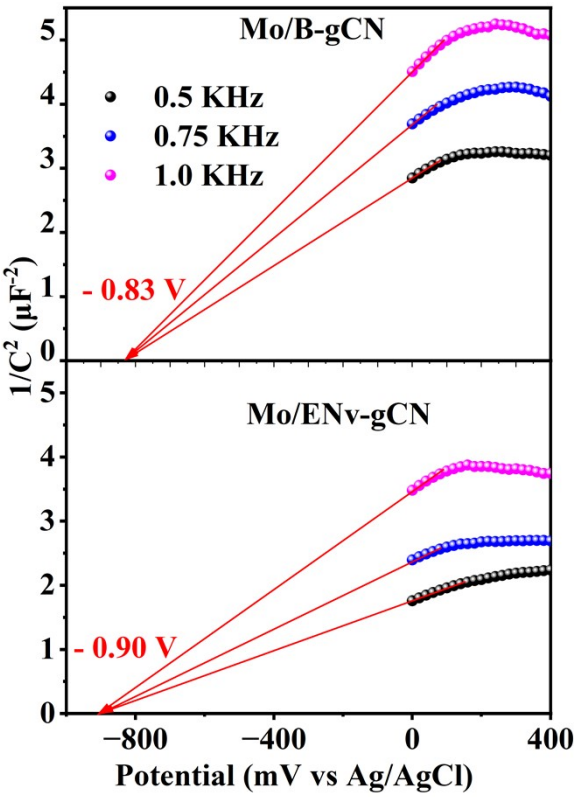

Fig. S12. Mott-Schottky plot for both catalysts

Mott-Schottky analysis:

Multi-frequency Mott-Schottky (M-S) analysis at 0.5, 0.75, and 1.0 kHz for both samples further demonstrates the enhanced electronic conductivity of Mo/ENv-gCN. Using the standard Mott-Schottky relationship (equation I) for n-type semiconducting materials, the donor density (N_D) of both samples was measured as shown in the Table S1.

$$\frac{1}{C^2} = \frac{2}{e\varepsilon\varepsilon_0 N_D}(V - V_{fb} - \frac{K_B T}{e}) \quad \text{(I)}$$

C is the capacitance of the space-charge region, ε is the dielectric constant of the semiconductor, ε_0 is the permittivity of free space, e is the electron charge (1.602 10^{-19} Coulomb), N_D is the donor carrier densities (carriers/cm^3), V is the applied potential, V_{fb} is the flat band potential, $K_B T$ is the Boltzmann constant 1.38 10^{-23} JK^{-1}, and T is the absolute temperature in which $K_B T/e$ can be negligible because it is only 25 mV at room temperature. The carrier density, N_D, can be determined from the slope of the experimental $1/C^2$ vs V (M-S) plots. From the Fig. S11, it is evident that Mo/B-gCN shows a steeper slope compared to Mo/ENv-gCN, indicating a lower donor density, whereas Mo/ENv-gCN exhibits a lower slope across all potentials, suggesting its higher carrier concentration and improved electrical conductivity.[17]

Table S3: Donor density (N_D) value for both catalysts:

Catalyst	Frequency (kHz)	Slope (μF^{-2} mV^{-1})	N_D (carriers/cm^3)

Mo/B-gCN	0.75	0.00326	$6.17*10^{18}$
Mo/ENv-gCN	0.75	0.00198	$10.17*10^{18}$

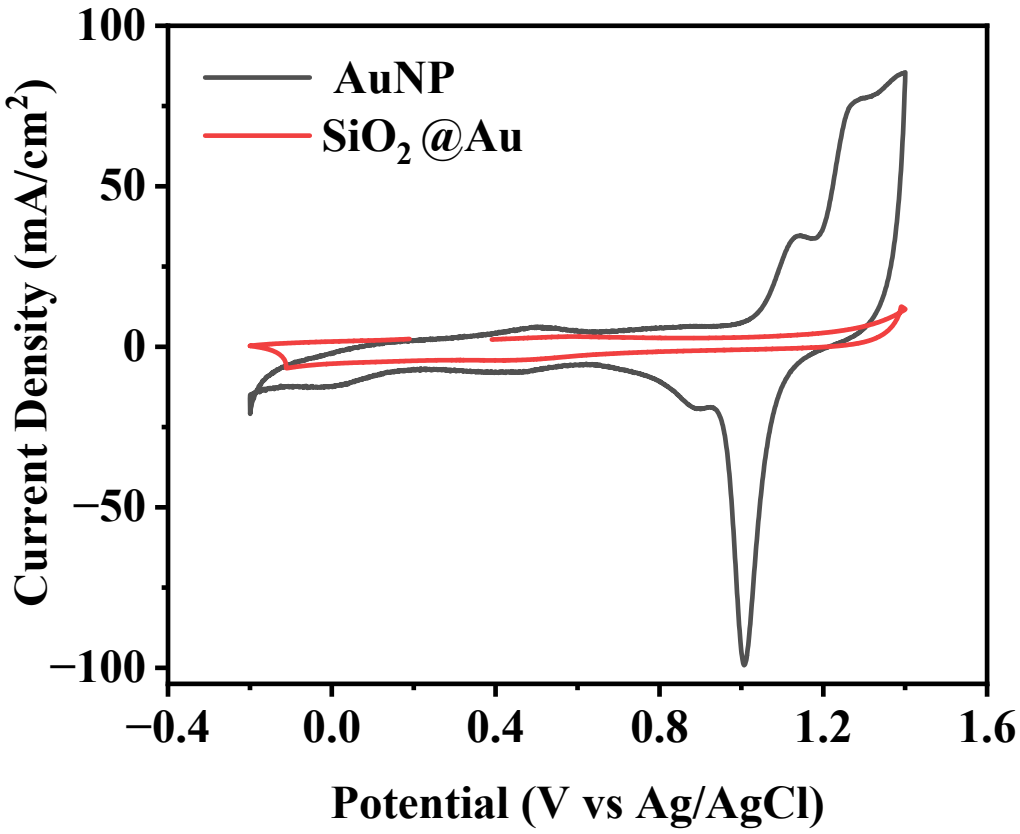

Fig. S13. Controlled CV experiments of AuNP and SiO_2@Au.

References

1 W. Wang, P. Xu, M. Chen, G. Zeng, C. Zhang, C. Zhou, Y. Yang, D. Huang, C. Lai, M. Cheng, L. Hu, W. Xiong, H. Guo and M. Zhou, *ACS Sustain. Chem. Eng.*, 2018, **6**, 15503–15516.

2 T. Hartman, C. S. Wondergem and B. M. Weckhuysen, *ChemPhysChem*, 2018, **19**, 2461–2467.

3 Y. Ren, H. Xiao, B. Chong, M. Xia, S. Kou, A. Xu, J. Li, J. Liu, H. Ou, Z. Ren and G. Yang, *Applied Catalysis B: Environment and Energy*, 2024, **353**, 124066.

4 M. Zheng, F. Zhou, H. Ma, X. Song and G. Wu, *RSC Adv.*, 2024, **14**, 36461–36470.

5 K. V. R. Chary, T. Bhaskar, G. Kishan and K. R. Reddy, *J. Phys. Chem. B*, 2001, **105**, 4392–4399.

6 Q. Hu, Y. Qin, X. Wang, Z. Wang, X. Huang, H. Zheng, K. Gao, H. Yang, P. Zhang, M. Shao and C. He, *Energy Environ. Sci.*, 2021, **14**, 4989–4997.

7 J. Wan, H. Zhang, J. Yang, J. Zheng, Z. Han, W. Yuan, B. Lan and X. Li, *Applied Catalysis B: Environment and Energy*, 2024, **347**, 123816.

8 S. Zhang, J. Wu, M. Zheng, X. Jin, Z. Shen, Z. Li, Y. Wang, Q. Wang, X. Wang, H. Wei, J. Zhang, P. Wang, S. Zhang, L. Yu, L. Dong, Q. Zhu, H. Zhang and J. Lu, *Nat. Commun.*, 2023, **14**, 3634.

9 M. Jiang, A. Tao, Y. Hu, L. Wang, K. Zhang, X. Song, W. Yan, Z. Tie and Z. Jin, *ACS Appl. Mater. Interfaces*, 2022, **14**, 17470–17478.

10 H. Du, H. Guo, K. Wang, X. Du, B. A. Beshiwork, S. Sun, Y. Luo, Q. Liu, T. Li and X. Sun, *Angew. Chem. Int. Ed.*, 2023, **62**, e202215782.

11 Q.-L. Hong, J. Zhou, Q.-G. Zhai, Y.-C. Jiang, M.-C. Hu, X. Xiao, S.-N. Li and Y. Chen, *Chemical Communications*, 2021, **57**, 11621–11624.

12 A. Adalder, S. Paul, N. Barman, A. Bera, S. Sarkar, N. Mukherjee, R. Thapa and U. K. Ghorai, *ACS Catal.*, 2023, **13**, 13516–13527.

13 Y. Huang, J. Long, Y. Wang, N. Meng, Y. Yu, S. Lu, J. Xiao and B. Zhang, *ACS Appl. Mater. Interfaces*, 2021, **13**, 54967–54973.

14 B. Yang, X. Ma, H. Wang, R. Yao, A. Li, Z. A, Z. Zheng, Y. Han and X. Ran, *ACS Sustain. Chem. Eng.*, 2026, **14**, 4148–4157.

15 Y. Wu, Y. Zhang, H. Zhao, Y. Peng, H. Ma, F. Kang, Z. Li, Y. Liu and Q. Zhang, *Chem. Sci.*, 2026, **17**, 4697–4705.

16 M. Zheng, Y. Wan, Z.-H. Huang, F. Kang and R. Lv, *Advanced Materials*, 2026, **38**, e14834.

17 I. Kunadian, S. M. Lipka, C. R. Swartz, D. Qian and R. Andrews, *J. Electrochem. Soc.*, 2009, **156**, K110.